Materials & Design 207 (2021) 109851

Contents lists available at ScienceDirect

Materials & Design

journal homepage: www.elsevier.com/locate/matdes

Modelling the influence of process parameters on precipitate formation in powder-bed fusion additive manufacturing of IN718

Jakub Mikula *, Rajeev Ahluwalia *, Robert Laskowski, Kun Wang, Guglielmo Vastola, Yong-Wei Zhang

*Institute of High Performance Computing, A*STAR, Singapore 138632, Singapore*

HIGHLIGHTS

- Two-scale simulation model predicts precipitation in 3D printed parts of complex geometry.
- Changing the process parameters can significantly influence precipitation process in 3D printed Inconel 718 alloy.
- The distribution of the precipitate nuclei in the as-built component depends on the shape of the component.
- Significant computational efficiency is gained by homogenizing the heat source at the level of a single stripe

GRAPHICAL ABSTRACT

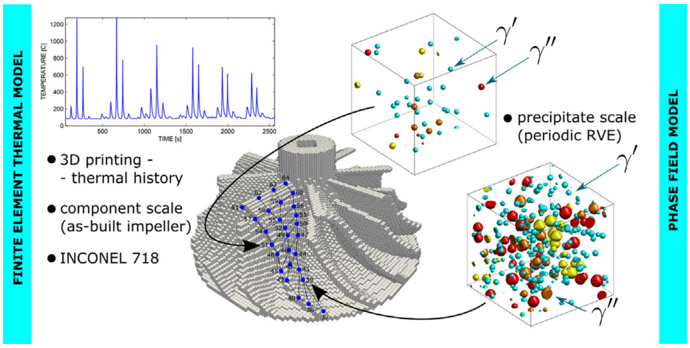

ARTICLE INFO

Article history:
Received 16 March 2021
Revised 21 May 2021
Accepted 21 May 2021
Available online 24 May 2021

Keywords:
Additive manufacturing
Precipitates
Phase field model
Inconel 718 alloy

ABSTRACT

In this work, we have developed a two-scale (finite element + phase field) model for simulating the precipitate evolution in IN718 in powder-bed fusion additive manufacturing. The thermal simulations at the scale of the component are resolved at the level of a single stripe of the scan path. This resolution allows to model various process parameters (or scan strategies) in complex geometry domains, here demonstrated by an impeller, and predicts the complete thermal history within each finite element layer. The predicted thermal history is in-full passed to multiple phase-field simulation representative volume elements (RVEs) that explicitly model the evolution of the γ' and γ'' precipitates in various locations of the impeller. We simulate the precipitate microstructures in different regions of the impeller and demonstrate the influence of process parameters on the volume fraction, size, and shape of the precipitates. Although no precipitates are found to form during the standard printing conditions (for instance EOS M290), we show that changing the process parameters such as stripe width or chamber temperature may induce significant precipitation in the as-built component.

1. Introduction

Powder-bed fusion additive manufacturing is a process during which the part is printed in a layer-by-layer fashion, by locally consolidating the powder of material that is melted using a concentrated heat source, such as a laser beam [1]. This process is of particular interest to engineering applications that require the production of complex monolithic shapes [2–4].

An extensively used class of metallic materials for additive manufacturing comprises of nickel-based superalloys, owing mainly to their weldability and excellent mechanical properties [5,6]. Given the material's ability to perform exceptionally well under high thermal and mechanical loadings, the alloy has been often employed in the applications such as turbine engines and

---

* Corresponding authors.
E-mail addresses: jakubm@ihpc.a-star.edu.sg (J. Mikula), rajeev@ihpc.a-star.edu.sg (R. Ahluwalia).

https://doi.org/10.1016/j.matdes.2021.109851
0264-1275/

nuclear reactors [7–9]. In the present work, the focus is specifically on INCONEL 718 (IN718). The microstructure of IN718 consists amongst others of the γ parent phase, δ precipitates and the γ' and γ'' precipitates of which the γ', γ'' are often exploited in strengthening the alloy [6,10]. These nanometer-sized spherical or disk-shaped precipitates usually strengthen the material through the mechanism of dislocation shearing [6]. In order to exploit the exceptional mechanical behaviour of the alloy, it is important to understand the formation of the γ', γ'' precipitates during the 3D printing process as well as during the post-build heat treatment.

Although additive manufacturing has excelled in producing components of geometrically complex shapes, tailoring the microstructure and the mechanical properties remains a challenge. While earlier efforts have focused mostly on altering the grain microstructures by exploring suitable printing strategies [11], we hypothesize that similar approaches may be also applied to altering the precipitate microstructures. In general, for IN718, the SLM (selective laser melting) process does not lead to formation of γ' and γ'' precipitates [12–14] and typically a post-build heat treatment is required to induce the precipitates. However, a recent experimental study by Yang et al. [15] provides supporting evidence demonstrating that in situ heat treatment during the build process can also lead to precipitation. Given the size of the precipitates and the complexity of the multiphysical phenomena, it is noticeable that exploring such strategies experimentally becomes difficult. Multi-physics models, however, enable to probe the parameter space virtually with a high degree of spatial and temporal resolution. In the present work, we use a multiphysics approach to explore the conditions that can enhance precipitation during the additive manufacturing process.

Numerical simulations of the temperature evolution during the layer-by-layer addition of material are usually performed using the Finite Element Method (FEM) [16]. However, performing such simulations for the whole component imposes a computational challenge that requires handling a large number of degrees of freedom. In fact, while a typical component has the size in the order of $\sim$10cm, the layer thickness remains very small, nominally, 40μm [17]. Therefore, brute-force simulations whereby each layer is resolved with a single finite element layer remain computationally intractable, if not impossible. As a result, the community has explored other approaches to effectively reduce the computational cost of the simulation. Hodge et al. developed an approach where multiple printed layers are lumped together and modelled as a single finite element layer [18,19]. In the same approach, the laser heat source is also lumped in an equivalent heat source which covers one layer in a few scan passes. Another approach is to model the heat source by activating a uniform "hot" layer of mesh elements at once, without the details of the laser passes [20]. Anderson et al. adopted the property switching element method in which the properties of finite elements are switched between gas or metal [21]. Other authors have carried out similar simulations to predict the thermal field cycles and residual stresses at part-scale [21–23].

A handful of multiscale approaches investigating the precipitate formation during printing have been developed. Most of these works have adopted the mean-field approach. Basoalto et al. [24] developed a multiscale approach to investigate the nucleation and dissolution of the precipitates in a simple cuboidal component for both CM247LC and IN718. A similar study has been carried out by Anderson et al. [21]. Promoppatum et al. [22] investigated the precipitation using a CCT diagram coupled with the predicted thermal histories. Although these studies predict precipitate evolution during printing, they are mean-field in nature and do not explicitly simulate the inhomogeneous distribution of precipitates in the matrix. On the other hand, phase field models can simulate the heterogeneous precipitate microstructure. Recently, these models have been used to simulate the precipitate evolution for Nickel-based superalloys [25–27]. In the present work, a phase field model is used to simulate the precipitate evolution during the printing process as well as during the post-build heat treatment.

While earlier works have been concerned mostly with simple geometries, the present work aims to develop a method to investigate precipitate evolution within the volume of complex geometry. In this work, we propose a sequential two-scale computational framework of the powder-bed fusion process applied to a complex geometry of an impeller shape to evaluate the thermal histories and the formation of the γ' and γ'' precipitates in IN718. We first present the component scale finite element model that predicts the thermal histories. We then continue by presenting the temperature dependent phase field model of the γ' and γ'' precipitates. The two scales are bridged using the temperature field $\theta(\boldsymbol{x}, t)$, that is an output of the thermal simulation model and an input to the precipitate model. In conjunction with the predicted thermal histories, we analyse the precipitate microstructure throughout the component under various printing conditions and conclude our analysis with the subsequent heat treatment simulations.

2. Thermal simulation at the component scale

2.1. Finite element model

For demonstration purposes, we choose the geometry represented by the open-source centrifugal impeller STL file [28] shown in Fig. 1. The diameter of the impeller is $d = 65$mm and the height of the impeller is $h = 31$mm.

The domain of the STL file is first discretized into voxels that are interpolated using suitable shape functions to form the isoparametric finite elements. The voxelization algorithm and the visualization tools are written using the open-source VTK library functions [29] as part of a larger in-house C++ code. The voxelized domain of the size of $80 \times 80 \times 80$ voxels that is used for the thermal simulations is shown in Fig. 2.

The temperature field $\theta(\boldsymbol{x}, t)$ is calculated by solving the heat equation assuming the heat flow through conduction and convection from the surface:

Fig. 1. Centrifugal impeller STL file domain used for the thermal simulation at the component scale. Open source STL file is obtained from [28]. The diameter of the impeller is $d = 65$ mm and the height of the impeller is $h = 31$ mm.

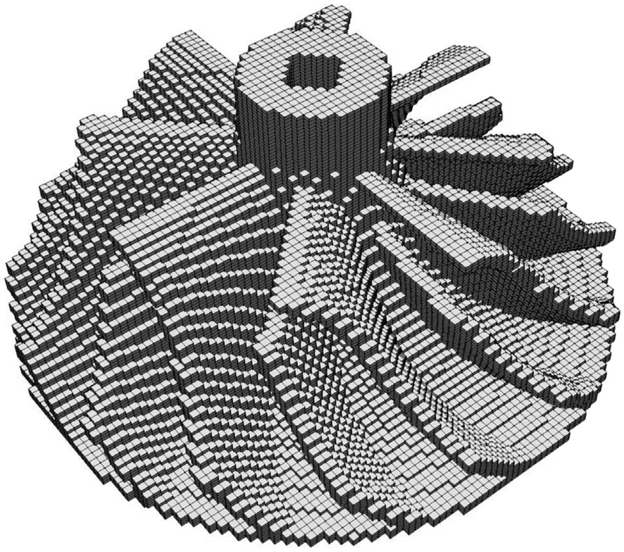

Fig. 2. Voxelized STL file domain within a box of 80 × 80 × 80 cells.

$$\rho c_p \frac{\partial \theta}{\partial t} = \nabla \cdot (k \nabla \theta) + Q, \tag{1}$$

where the material parameters are specified in Table 2. The convective heat transfer on the surface is defined through $q_h = h(\theta - \theta_\infty)$ boundary condition, where θ is the temperature at the interface, θ_∞ is the chamber temperature and h is the convection coefficient.

The finite element approximation yields a system of linear differential equations that can be written in the following form

$$\boldsymbol{M}\dot{\theta} + \boldsymbol{K}\theta = \boldsymbol{Q} - \boldsymbol{H}_\Gamma(\theta - \theta_\infty), \tag{2}$$

where $\boldsymbol{M}$ is the capacitance matrix, $\boldsymbol{K}$ is the conductance matrix, $\boldsymbol{Q}$ is the heat source vector, and $\boldsymbol{H}_\Gamma$ is the contribution due to the convection from the surface Γ that is divided into the surface of the substrate (bottom) and the remaining surface (powder). The global matrices are assembled from the isoparametric tetrahedral finite elements with bi-linear shape functions. The convection at the surface is approximated using quadrilateral finite elements with bilinear shape functions.

The system of differential equations is solved using the fully implicit Euler method that reduces into a linear system of equations,

$$\mathscr{K}\theta^{t+\Delta t} = \mathscr{F}, \tag{3}$$

for each time step Δt. Here, $\mathscr{K}$ represents the global matrix, and $\mathscr{F}$ is the global vector. Their explicit expressions are written below:

$$\begin{aligned} \mathscr{K} &= \boldsymbol{M} + \alpha\Delta t(\boldsymbol{K} + \boldsymbol{H}_\Gamma) \\ \mathscr{F} &= \{\boldsymbol{M} - (1-\alpha)\Delta t[\boldsymbol{K} + \boldsymbol{H}_\Gamma]\}\theta^t + \Delta t\left[(1-\alpha)\boldsymbol{Q}^t + \alpha\boldsymbol{Q}^{t+\Delta t}\right]. \\ &\quad + \Delta t \boldsymbol{H}_\Gamma \theta_\infty \end{aligned} \tag{4}$$

For $\alpha \geqslant 0.5$, the method is unconditionally stable, here $\alpha = 1$. The solver for the linear system of equations (Eq. 3) is MPI parallelized using an iterative solver based on the package Trilinos [30]. The assembly of the heat source term $\boldsymbol{Q}$ is detailed in the section below.

2.2. Heat source model

In comparison to other studies that have assumed either a lumped heat source model or a two-scale simulation approach as detailed in Introduction, here, we propose to model the heat source at the scale of a single stripe. This approach provides an additional level of resolution while still remaining computationally tractable. A schematic of the model is presented in Fig. 3. The exact scan path consists of single scan vectors (shown by the small arrows) separated by the distance of hatch spacing along the direction of the scan stripe. The stripes are separated by the distance of stripe width. Aiming to resolve the heat source at the level of the stripes, it is necessary to account for the single scan vectors in a homogenized way. This is achieved by prescribing an elliptical Gaussian heat source intensity that is schematically shown in Fig. 3.

The heat intensity $I(x,y,z)$ of the volumetric heat source with exponential decay is then defined as:

$$\begin{aligned} I(x,y,z) &= \frac{AP}{2\pi\sigma_x\sigma_y d_0} E_1 E_2 \\ E_1 &= e^{-\left[a(x-x_0)^2 + 2b(x-x_0)(y-y_0) + c(y-y_0)^2\right]}, \\ E_2 &= e^{\left[-\frac{z_0 - z}{d_0}\right]} \end{aligned} \tag{5}$$

where A is the absorptivity coefficient, P represents the laser power, d_0 represents the strength of the decay, and σ_x and σ_y are related to the width and height of the ellipse. The location of the heat source is defined by the $[x_0, y_0, z_0]$ coordinates. The aspect ratio of the ellipse is determined from the scan path parameters, mainly the stripe width and the hatch spacing ($\sigma_x \sim$ stripe width, $\sigma_y \sim$ hatch spacing).

The coefficients a, b, and c that prescribe the orientation of the ellipse in Eq. 5 are defined as:

$$\begin{aligned} a &= \frac{\cos^2\Theta}{2\sigma_x^2} + \frac{\sin^2\Theta}{2\sigma_y^2} \\ b &= -\frac{\sin 2\Theta}{4\sigma_x^2} + \frac{\sin 2\Theta}{4\sigma_y^2}, \\ c &= \frac{\sin^2\Theta}{2\sigma_x^2} + \frac{\cos^2\Theta}{2\sigma_y^2} \end{aligned} \tag{6}$$

where Θ is the orientation of the stripe with respect to the global coordinate system.

We should note that the height of the simulated finite element layer h^{FEM} is larger than the height of the real physical layer h, in this example $h^{\text{FEM}}/h \approx 10$. While this is a necessary step in order to keep the computational time feasible, it is ensured in the simulation that the total energy used for building the component is the same regardless of the number of finite element layers. This condition can be satisfied by re-scaling the velocity (or the power of the heat source) by the factor of h^{FEM}/h. The heat intensity I is prescribed to each Gauss integration point during the assembly process of the global vector $\boldsymbol{Q}$.

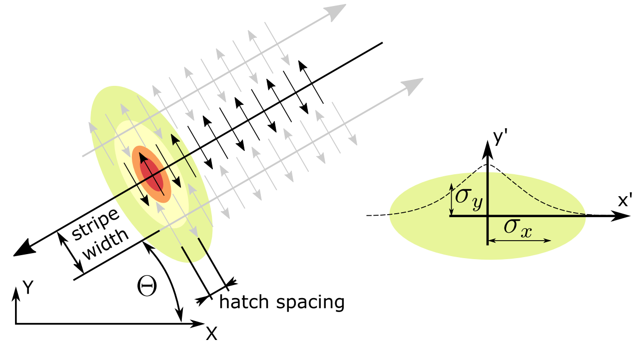

Fig. 3. A schematic of the heat source homogenization with the resolution at the level of a single stripe. The parameters of the elliptical Gauss function are shown on the right.

2.3. Printer settings

It is well known that, in contrast to subtractive manufacturing processes, additive manufacturing possesses the inherent advantage of having the flexibility to tailor the printing process parameters in an effort to produce structurally sound, reliable, and high-performance parts. Therefore, we incorporate multiple printer parameters into the simulation framework that are used to generate the scan path. The printer parameters and the printer settings used for the simulation are summarized in Table 1.

We first aim to establish the framework by investigating the effect of a few selected printer parameters. Here, one set of parameters is focused on the effect of the stripe width, while the other set of parameters is focused on the effect of the chamber temperature. In total, five printer set-ups are investigated: (S1) standard printing settings (for instance EOS M290 [12]), and non-standard settings with (NS1) reduced stripe width from 10 mm to 5 mm, (NS2) reduced stripe width from 10 mm to 2 mm, (NS3) increased chamber temperature from 80° to 400°, and (NS4) increased chamber temperature from 80° to 600°.

The scan path generated for the standard setting S1 is shown in Fig. 4. The figure overlaps the original stl file with the individual stripes that are plotted using the red lines. The stripes are incrementally reoriented by 67 degrees with each new finite element layer. The stripe width for the standard printing conditions is 10 mm.

For a comparison, Fig. 5 depicts the scan path generated for the reduced stripe width of 2 mm that clearly shows a higher density of scan passes within each layer. The process of generating the scan path within the developed C++ code is automated and can be applied to any other stl file.

While the aim of this work is to discern the role of the five selected printing conditions, we note that the parameter space (Table 1) offers a large playground to investigate the optimal processing window that will be explored in the future work.

2.4. Material parameters

The material parameters of a generic IN718 used in the part-scale simulations are listed in Table 2.

It is noteworthy that the dissipation q_h through the bottom base plate and the powder is modelled using the heat convection boundary conditions instead of explicitly resolving the powder or the base plate. This is motived by reducing the overall computational costs of the simulation. Here, $q_h = h(\theta - \theta_\infty)$, where θ is the temperature of the interface, θ_∞ is the chamber temperature, and h is the convection coefficient. In this work, we attribute a higher convection coefficient to the bottom surface because the base plate, as opposed to the powder, is made of fully dense metal. It is also straightforward within the developed finite element frame-

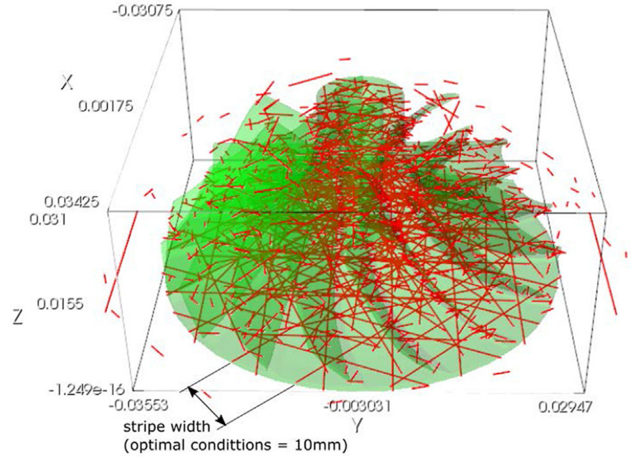

Fig. 4. Individual stripes of the scan path. The stripe width for the default printing conditions is 10 mm.

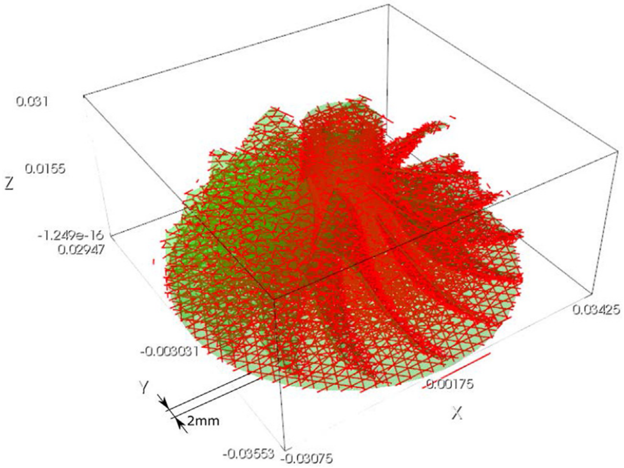

Fig. 5. Individual stripes of the scan path. The stripe width is set to 2 mm.

Table 2
Material parameters used in the thermal simulation for a generic Inconel 718 alloy.

symbol	variable	unit	generic IN718
c_p	specific heat	$\frac{J}{kg \cdot K}$	435
k	thermal conductivity	$\frac{W}{m \cdot K}$	11.2
ρ	density	kg/m^3	7734
h_{powder}	convection coefficient - powder	$\frac{W}{m^2 \cdot K}$	10
h_{bottom}	convection coefficient - bottom	$\frac{W}{m^2 \cdot K}$	600

Table 1
Printer settings for the standard and non-standard printing conditions. The deviations from the standard case are highlighted for each column.

variable	unit	value				
		S1	NS1	NS2	NS3	NS4
stripe width	mm	10	***5***	***2***	10	10
hatch spacing	mm	0.11	0.11	0.11	0.11	0.11
scan speed	m/s	0.96	0.96	0.96	0.96	0.96
layer thickness	mm	0.04	0.04	0.04	0.04	0.04
reacoater time	s	15	15	15	15	15
heat source absorption	-	0.65	0.65	0.65	0.65	0.65
initial stripe orientation	DEG	0	0	0	0	0
incremental stripe orientation	DEG	67	67	67	67	67
scan passes per layer	-	1	1	1	1	1
chamber temperature	°C	80	80	80	***400***	***600***
power	W	285	285	285	285	285

work to account for the surrounding powder explicitly by modelling it as a continuum with its properties derived from the fractional porosity. However, evaluation of the thermal transport at the scale of the powder particle would require an additional simulation length-scale that is out of the scope of this study.

2.5. Results of thermal simulation

In this section, we discuss the results of the finite element simulations at the component scale for the five studied cases listed in Table 1. The collage in Fig. 6 displays the temperature field evolution during the layer-by-layer assembly process of the impeller using the standard printing conditions (see case S1 in Table 1). For better visualization of the heat-affected zone near the heat source, the color map is capped at 600 °C. The direction of the moving heat source (following the scan path in Fig. 4) can be recognized by the elongated temperature profile also emphasized using the white arrows in Fig. 6a) and Fig. 6b). The ellipse-like distribution of the temperature field in the direction perpendicular to the moving heat source is due to the implemented elliptical Gauss heat source homogenization smearing out the effect of single scan vectors by resolving the heat source at the level of each stripe. The computational time of this thermal simulation is relatively short, approximately two hours (2 *Intel(R) Xeon(R) CPU E5-2699 v4 @ 2.20 GHz*, 22 cores each), that is shorter than the total physical printing time of the impeller that is about four hours.

The thermal simulation predicts a complete thermal history for each node of the finite element mesh that is stored into a binary file (~10.3 GB). The predicted thermal history for the node located near the bottom of the impeller is shown in Fig. 7. For better visualization, a magnification of the thermal history in the time interval of 2500s resolving the first six peaks is also embedded within the same figure. The transition temperatures for γ' and γ'' precipitates are highlighted using the dashed lines.

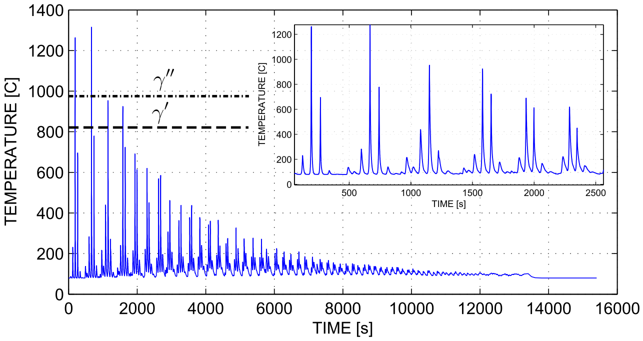

Fig. 7. The complete thermal history for the node 2960 (interpolation point id: 0) near the bottom-center of the impeller (see Fig. 11). The smaller plot represents the magnification of the first six peaks. The two dashed lines in the figure represent the γ' and γ'' transient temperatures.

Each of the larger spikes can be attributed to the advancement of the heat source along the build direction to a new finite element layer. The smaller peaks in the neighbourhood of the larger ones can be attributed to the movement of the heat source along the stripes within each layer. Additionally, Fig. 15 in Appendix A demonstrates how the peak density changes at different printing conditions.

The thermal history for the node located near the top of the impeller is shown in Fig. 8. Similarly, a magnification within the time interval of 2500s is embedded within the figure for a better resolution.

While the temperature profile near the bottom of the impeller shows, on average, exponential decay with the advancement of the heat source along the build direction, the thermal cycles in the upper region of the shaft become more randomized. This is due to the shape of the shaft which is of a much smaller diameter than the bottom of the impeller, making the time intervals between the adjacent layers much shorter. It should be noted that due to the homogenization of the scan vectors (see Fig. 3), the temperature near the meltpool cannot be predicted correctly. The

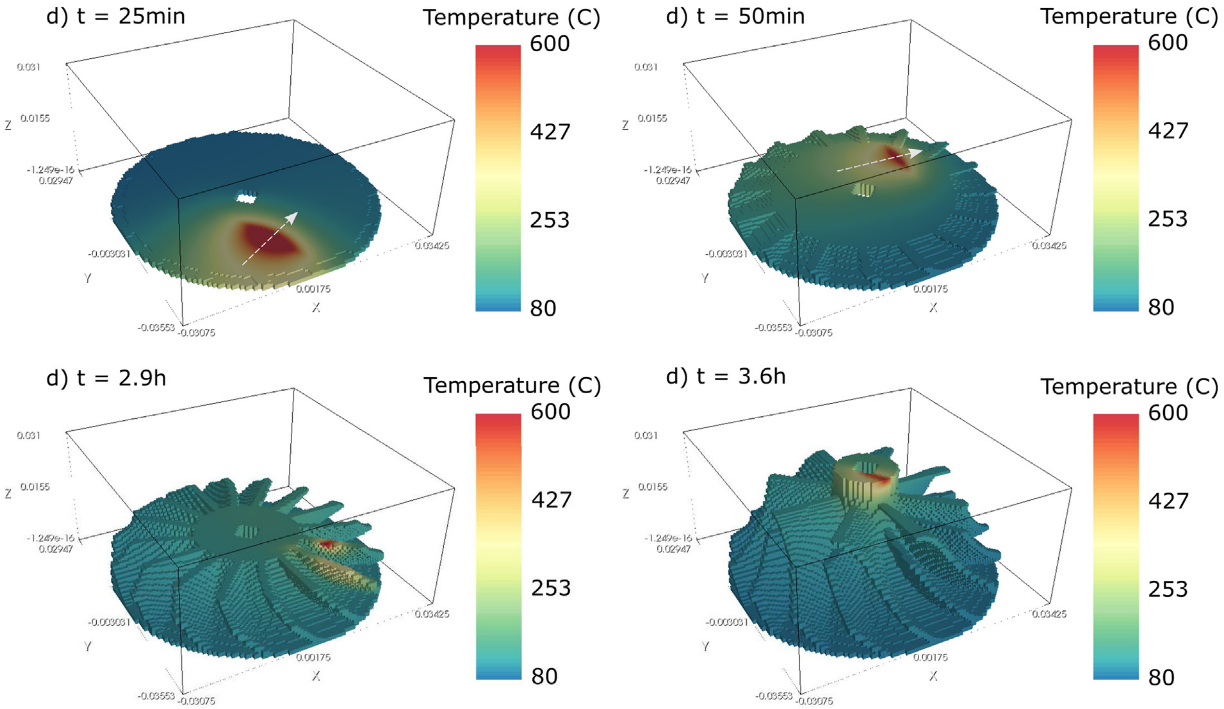

Fig. 6. Thermal solver simulation result showing the temperature field during the layer-by-layer building process. The color map is capped at 600 °C to better visualize the temperature field near the heat source. The total physical printing time is less than 4 h. The scan path of this process is visualized in Fig. 4.

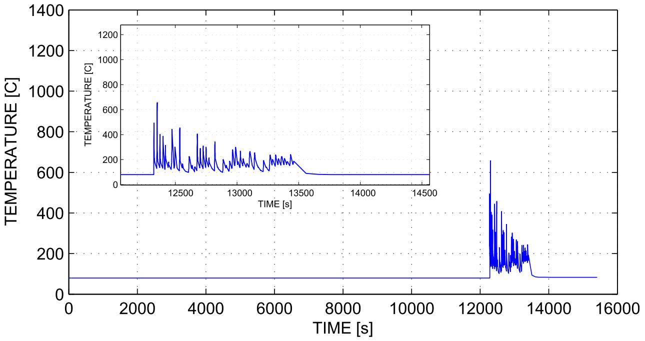

Fig. 8. The complete thermal history for the node 139076 (interpolation point id: 36) near the top of the impeller (see Fig. 11). The embedded plot magnifies the thermal history in the time interval of 2500s (for comparison, see Fig. 7).

finite element size in this simulation is 0.81mm in the transverse direction and 0.39mm in the build direction, while the size of the meltpool is one order of magnitude smaller [11]. Although lacking the description of the temperature field within the close proximity of the meltpool, we note that the emphasis of the study is on the overall thermal history covering the length-scale and time-scale of the whole component that is necessary in order to predict the formation of precipitates. Resolution of the meltpool would otherwise require an additional level of simulation scale that is out of the scope of this study. The thermal histories for other printing conditions are collated in Appendix A in Fig. 15. A movie for the case with the stripe width of 2 mm is provided in the supplementary information.

To visually assess the temperature profile near the moving heat source, Fig. 9 displays the comparison of the temperature field for the case with a 10 mm stripe width and a 2 mm stripe width. For better visualization, the color map is capped at 600 °C. The arrow in the figure indicates the moving direction (that is the same in both cases). Clearly, the temperature field in the 10 mm case develops into an ellipse extended perpendicularly to the moving direction, while in the 2 mm case, the temperature profile becomes elongated along the moving direction and starts to resemble the solution for a moving point heat source [31].

We have demonstrated that despite the complex geometry, the simulations are relatively fast (in comparison to the real printing time), yet achieving a great amount of detail. Higher resolutions can be achieved at the component scale by increasing the number of voxels (finite element layers); however, at the expense of the computational cost.

The next section introduces the phase field model of γ' and γ'' precipitates. The complete thermal history for the selected nodes presented in this section is then passed to the lower-level phase field simulations to investigate the precipitate evolution during the printing stage. The advantage of using the phase field models lies in the explicit resolution of the precipitate shape, size and distribution.

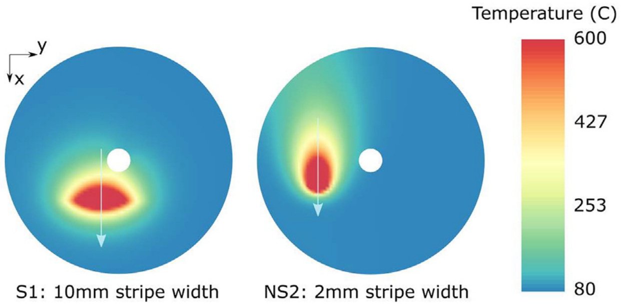

Fig. 9. Comparison of the temperature field distribution near the heat source in the first finite element layer for the cases with the stripe width of 10 mm and 2 mm. The arrow indicates the heat source direction.

3. Precipitate phase field simulations

3.1. Phase field model

The phase field model for IN718, incorporating the γ' and γ'' product phases is formulated in terms of a four component vector order parameter $\vec{\eta} = (\eta_1, \eta_2, \eta_3, \eta_4)$. The parent γ phase is defined as $\vec{\eta} = (0,0,0,0)$, whereas the single variant of γ' is defined by $\vec{\eta} = (\eta,0,0,0), \eta > 0$. Similarly, the three variants of γ'' are defined as $\vec{\eta} = (0,\eta,0,0), \vec{\eta} = (0,0,\eta,0)$ and $\vec{\eta} = (0,0,0,\eta)$. The total free energy is constructed as shown below:

$$\mathscr{F} = \int_V [f_{int} + f_{chem} + f_{el}] dV. \tag{7}$$

The interfacial energy density contribution f_{int} is considered as:

$$f_{int} = W_{\gamma'} \eta_1^2 (1-\eta_1)^2 + \tfrac{K_{\gamma'}}{2} (\nabla \eta_1)^2 + \sum_{j=2}^{4} \left[W_{\gamma''} \eta_j^2 (1-\eta_j)^2 + \tfrac{K_{\gamma''}}{2} \left(\nabla \eta_j \right)^2 \right] + \xi \sum_{i \neq j} \eta_i^2 \eta_j^2. \tag{8}$$

Here, the quantities $W_{\gamma'}, W_{\gamma''}$ are the barrier heights, and $K_{\gamma'}, K_{\gamma''}$ are the gradient coefficients. These quantities are computed from the prescribed interfacial energies and suitable interfacial widths between the parent and the product phase [25]. The parameter ξ is chosen large enough to ensure that only the order parameter that describes the given phase is non-zero.

The chemical energy density contribution is formulated as:

$$f_{chem} = \tfrac{1}{V_m} \left[\left(1 - \sum_{j=1}^{4} h(\eta_j) \right) G_\gamma (\chi_{Al}^{\gamma}, \chi_{Nb}^{\gamma}) + h(\eta_1) G_{\gamma'} (\chi_{Al}^{\gamma'}, \chi_{Nb}^{\gamma'}) + \left(\sum_{j=2}^{4} h(\eta_j) \right) G_{\gamma''} (\chi_{Al}^{\gamma''}, \chi_{Nb}^{\gamma''}) \right]. \tag{9}$$

Here $h(\eta_i) = \eta_i^3 (6\eta_i^2 - 15\eta_i + 10)$ is an interpolation function, V_m is the molar volume, and $G_\gamma, G_{\gamma'}$ and $G_{\gamma''}$ are the temperature-dependent Gibbs free energies of the phases. In reality IN718 is a multi-component alloy. Incorporating all the components into the model is a numerically challenging task. Therefore, a surrogate ternary approximation is adopted. An alloy system (Ni-{Al}-{Nb}) is considered, where {Al} represents γ' stabilizers, {Nb} represents γ'' stabilizers. A thermodynamic database developed for this surrogate system is used in the present work (see Laskowski et al. [27] for more details).

Following [32], the auxiliary composition variables are represented by $\chi_{Al}^{\gamma}, \chi_{Nb}^{\gamma}, \chi_{Al}^{\gamma'}, \chi_{Nb}^{\gamma'}, \chi_{Al}^{\gamma''}, \chi_{Nb}^{\gamma''}$. The auxiliary compositions for all phases are obtained by solving the following set of equations:

$$\begin{aligned} \frac{\partial G_\gamma}{\partial \chi_{Al}^{\gamma}} &= \frac{\partial G_{\gamma'}}{\partial \chi_{Al}^{\gamma'}} = \frac{\partial G_{\gamma''}}{\partial \chi_{Al}^{\gamma''}} = \mu_{Al,Ni} \\ \frac{\partial G_\gamma}{\partial \chi_{Nb}^{\gamma}} &= \frac{\partial G_{\gamma'}}{\partial \chi_{Nb}^{\gamma'}} = \frac{\partial G_{\gamma''}}{\partial \chi_{Nb}^{\gamma''}} = \mu_{Nb,Ni} \end{aligned}, \tag{10}$$

and

$$\begin{aligned} \chi_{Al} &= \left(1 - \sum_{j=1}^{4} h(\eta_j) \right) \chi_{Al}^{\gamma} + h(\eta_1) \chi_{Al}^{\gamma'} + \left(\sum_{j=2}^{4} h(\eta_j) \right) \chi_{Al}^{\gamma''} \\ \chi_{Nb} &= \left(1 - \sum_{j=1}^{4} h(\eta_j) \right) \chi_{Nb}^{\gamma} + h(\eta_1) \chi_{Nb}^{\gamma'} + \left(\sum_{j=2}^{4} h(\eta_j) \right) \chi_{Nb}^{\gamma''} \end{aligned}. \tag{11}$$

Here χ_{Al}, χ_{Nb} are the actual compositions, and $\mu_{Al,Ni}$ and $\mu_{Nb,Ni}$ are the diffusion potentials.

The transformation also leads to elastic strains that arise due to the lattice misfit between the parent (γ) and the product (γ', γ'') phases. The elastic energy density is:

$$f_{el} = \frac{1}{2}\sum_{ijkl} C_{ijkl} e_{ij} e_{kl}, \tag{12}$$

where the elastic tensor C_{ijkl} and strain tensor e_{ij} fields are:

$$C_{ijkl} = \left(1 - \sum_{m=1}^{4} h(\eta_m)\right) C^{\gamma}_{ijkl} + h(\eta_1) C^{\gamma'}_{ijkl} + \left(\sum_{m=2}^{4} h(\eta_m) C^{\gamma''_m}_{ijkl}\right), \tag{13}$$

$$e_{ij} = \varepsilon_{ij} - h(\eta_1)\varepsilon^{\gamma'}_{ij} - \left(\sum_{m=2}^{4} h(\eta_m)\varepsilon^{\gamma''_m}_{ij}\right) - \delta_{ij}\varepsilon^{th}. \tag{14}$$

Here, ε^{v}_{ij} represents the transformation strain tensor associated with the v-th variant of the precipitate phase, ε^{th} represents the thermal strain, and ε_{ij} is the linearized strain tensor defined as $\varepsilon_{ij} = 1/2((\partial u_i)/(\partial x_j) + (\partial u_j)/(\partial x_i)) + \bar{\varepsilon}_{ij}$. The strain $\bar{\varepsilon}_{ij}$ components are adjusted such that the simulation cell remains on average stress-free. The thermal strain is calculated using the method provided in reference [27].

The transformation kinetics of the system is described by the standard set of phase field equations that are coupled with the multi-component diffusion equations:

$$\frac{1}{\Gamma_i}\frac{\partial \eta_i}{\partial t} = -\frac{\delta \mathscr{F}}{\delta \eta_i}, \tag{15}$$

$$\begin{aligned} \frac{\partial \chi_c}{\partial t} &= -\nabla \cdot \left(\sum_{c' \neq Ni} L_{cc'} \nabla \mu_{c',Ni}\right) \\ L_{cc'} &= \sum_{c''} (\delta_{cc'} - \chi_c)(\delta_{c'c''} - \chi_{c'})\chi_{c''} M_{c''} \end{aligned}, \tag{16}$$

while also enforcing the mechanical equilibrium

$$\frac{\partial \sigma_{ij}}{\partial x_i} = 0, \sigma_{ij} = \frac{\partial f_{el}}{\partial \varepsilon_{ij}}. \tag{17}$$

Eq. 15 describes the evolution of the i^{th} precipitate order parameter associated with its interfacial mobility Γ_i. Eq. 16 is the multi-component diffusion equation [33] where the concentration dependent mobility $L_{cc'}$ is calculated from the temperature-dependent atomic mobility M_c obtained from kinetic databases. The mechanical equilibrium equation is used to calculate the displacement field and the associated stress/strain field.

Table 3 summarizes the material parameters for INCONEL 718 used in the phase field simulations.

Table 4 shows the transformation strains for the γ' and γ'' precipitates, expressed in the basis of the parent phase. The three variants of γ'' are obtained by a permutation of the diagonal elements.

Table 5 shows the elastic tensors for the γ' and γ'' precipitates used in the simulations.

Table 3
Material properties of INCONEL 718 used in the phase field simulations.

symbol	variable	unit	value
G_v	molar Gibbs free energies	$\frac{\mathrm{J}}{\mathrm{mol}}$	surrogate ternary database, following [27]
$K_{\gamma'}$	gradient coefficient	$\frac{\mathrm{J}}{\mathrm{m}}$	$6.2 \cdot 10^{-10}$ [25]
$K_{\gamma''}$	gradient coefficient	$\frac{\mathrm{J}}{\mathrm{m}}$	$1.24 \cdot 10^{-9}$ [25]
$W_{\gamma'}$	barrier height	$\frac{\mathrm{J}}{\mathrm{m}^3}$	$7.45 \cdot 10^{7}$ [25]
$W_{\gamma''}$	barrier height	$\frac{\mathrm{J}}{\mathrm{m}^3}$	$1.49 \cdot 10^{8}$ [25]
$\gamma_{\gamma'}$	interfacial energy	$\frac{\mathrm{J}}{\mathrm{m}^2}$	0.0505 [25]
$\gamma_{\gamma''}$	interfacial energy	$\frac{\mathrm{J}}{\mathrm{m}^2}$	0.105 [25]
ξ	coupling coefficient	$\frac{\mathrm{J}}{\mathrm{m}^3}$	$1.07 \cdot 10^{11}$ [25]
M_c	atomic mobility	$\frac{\mathrm{mol}}{\mathrm{N \cdot s \cdot m^2}}$	following [27]
Γ_v	interfacial mobility	$\frac{\mathrm{m}^2}{\mathrm{N \cdot s}}$	$5.57 \cdot 10^{-1} \exp(-\frac{19098}{T})$

Table 4
Transformation strains for γ' and γ'' precipitates, expressed in the basis of the parent phase [25]. The three variants of γ'' are obtained by permutation of the diagonal elements.

$\begin{bmatrix} -0.003 & 0 & 0 \\ 0 & -0.003 & 0 \\ 0 & 0 & -0.003 \end{bmatrix}_{\gamma'}$	$\begin{bmatrix} 0.0286 & 0 & 0 \\ 0 & 0.0067 & 0 \\ 0 & 0 & 0.0067 \end{bmatrix}_{\gamma''_1}$
	+ γ''_2, γ''_3 symmetry-equivalent tensors

The model described by Eqs. 7–17 with its parameters stated in Tables 3–5 is used to simulate the precipitate evolution during additive manufacturing. It should be pointed out that, unlike reference [27], a temperature-dependent interfacial mobility has been considered in the present work. In general, the experimental data for interfacial mobilities are not available. Instead, a common practice is to set the interfacial mobility large enough so that the kinetics is dominated by the diffusion equation. However, very large interfacial mobilities can lead to unphysical growth conditions in the simulations, particularly at lower temperatures. Therefore, the interfacial mobility is chosen such that unphysical growth conditions at lower temperatures may be avoided. In the present work, the temperature dependent optimum interfacial mobilities are fitted to an Arrhenius form (see Table 3).

It should be noted that the precipitate gradation in this work is purely driven by the thermal history, whereas in reality, the gradation may also occur due to the compositional segregation that may lead to the formation of additional phases such as delta or Laves phases that were neglected in the current simulation.

3.2. Simulation of precipitate evolution during printing

During the build process, each location undergoes a sequence of rapid heating–cooling cycles, as can be observed in Fig. 7. It is clear that, during the build, the temperature at a given location crosses the γ' and γ'' formation temperatures several times. Further, the thermal history can be different in different regions of the component that is being built. The thermal history can also be controlled by the underlying process parameters. Therefore, it is important to understand how precipitate growth can vary at different locations in the part as well as how it can be controlled by the process parameters. Understanding the role played by process parameters is also crucial for developing new printing strategies that may lead to parts with superior mechanical properties. In this section, we use phase field simulations in conjunction with the part-scale thermal model to simulate the precipitate formation for the impeller introduced in Section 2.

An important ingredient of a precipitate growth model is a nucleation model that determines how many precipitates are nucleated at a given time and temperature. In the present work, we use the classical nucleation theory. Following Laskowski et al. [27], the nucleation rates $J_{\gamma'}$ and $J_{\gamma''}$ are chosen such that the simulated Time-Transformation-Temperature (TTT) curves are consistent with the typical experimentally observed curves. The nuclei are seeded according to probabilities that can be computed in terms of the nucleation rates as $P_{\gamma'} = 1 - \exp(-J_{\gamma'}\Delta t \Delta V)$ and $P_{\gamma''} = 1 - \exp(-J_{\gamma''}\Delta t \Delta V)$, where Δt is the time step and ΔV is the volume associated with the grid spacing. Numerically, at each grid point and instant, random numbers r_i between 0 and 1 are generated (here i refers to the phase). If $r_i < P_i$, then a spherical nucleus of the i-th phase with a radius of 15 nm is introduced. The size of the nuclei is determined such that first, the nucleation should be super-critical, that is, the nuclei should not shrink after the seeding, and second, its value should allow the resulting TTT diagrams to match with the experimental results. The underlying reason is

Table 5
Elastic constants for the γ parent phase, γ' precipitate and γ'' precipitates [GPa], expressed in the basis of the parent phase [34].

$$\begin{bmatrix} 276 & 159 & 159 & 0 & 0 & 0 \\ 159 & 276 & 159 & 0 & 0 & 0 \\ 159 & 159 & 276 & 0 & 0 & 0 \\ 0 & 0 & 0 & 132 & 0 & 0 \\ 0 & 0 & 0 & 0 & 132 & 0 \\ 0 & 0 & 0 & 0 & 0 & 132 \end{bmatrix}_{\gamma} \quad \begin{bmatrix} 238 & 147 & 147 & 0 & 0 & 0 \\ 147 & 238 & 147 & 0 & 0 & 0 \\ 147 & 147 & 238 & 0 & 0 & 0 \\ 0 & 0 & 0 & 129 & 0 & 0 \\ 0 & 0 & 0 & 0 & 129 & 0 \\ 0 & 0 & 0 & 0 & 0 & 129 \end{bmatrix}_{\gamma'} \quad \begin{bmatrix} 286 & 181 & 160 & 0 & 0 & 0 \\ 181 & 286 & 160 & 0 & 0 & 0 \\ 160 & 160 & 308 & 0 & 0 & 0 \\ 0 & 0 & 0 & 112 & 0 & 0 \\ 0 & 0 & 0 & 0 & 112 & 0 \\ 0 & 0 & 0 & 0 & 0 & 116 \end{bmatrix}_{\gamma''_1}$$

+ γ''_2, γ''_3 symmetry-equivalent tensors

that a different nucleus size can give rise to a different probability of seed shrinkage, which in turn changes the TTT diagrams.

Fig. 10 shows the temperature dependence of the maximum nucleation probability for both γ' and γ'' precipitates. These probabilities determine whether or not a given precipitate will form in a given temperature range, which will determine the final precipitate microstructure.

The precipitation is simulated using Eq. 7–17 and using the nucleation model discussed above. A phase field representative volume element (RVE) can be assigned to each physical point in the component and the associated thermal history can be used as an input to the phase field simulation. The thermal history data are cropped in t such that the peaks above the melting temperature are not considered as we do not model the remelting and solidification in this work. In the present work, by exploiting the geometrical similarities, we select 37 points in the middle cross-section and 28 points located on one of the larger blades. The selected points are illustrated in Fig. 11. For each of these points, a phase-field calculation is run using the thermal history obtained at part-scale, here provided as an input.

The results $\mathscr{R}$ of the phase field simulations, specifically, the number of γ' and γ'' nuclei, in between the adjacent points in Fig. 11 are found from the interpolation using the inverse distance weighting algorithm,

$$\mathscr{R}(\boldsymbol{x}) = \begin{cases} \dfrac{\sum_{i=1}^{N} w_i(\boldsymbol{x})\mathscr{R}_i}{\sum_{i=1}^{N} w_i(\boldsymbol{x})} & \text{if} \quad d(\boldsymbol{x}, \boldsymbol{x}_i) \neq 0 \\ \mathscr{R}_i & \text{if} \quad d(\boldsymbol{x}, \boldsymbol{x}_i) = 0 \end{cases}, \tag{18}$$

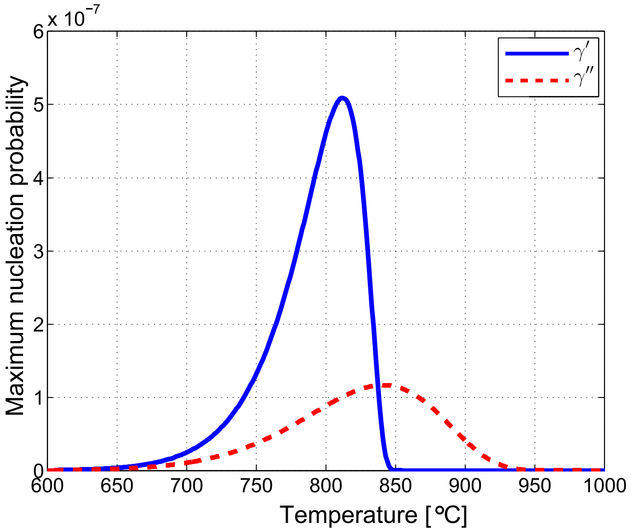

Fig. 10. Nucleation probabilities as a function of temperature.

where the weights are calculated as $w_i(\boldsymbol{x}) = 1/d(\boldsymbol{x}, \boldsymbol{x}_i)^p$ with d being the distance between the two points. This allows for a relatively simple implementation of interpolation in complex function domains.

The phase field equations are solved for each RVE using an iterative real space finite difference solver. Each RVE is assumed to be macroscopically stress-free and subjected to a periodic constraint. The size of the simulation RVE is $128 \times 128 \times 128$ grid points with a 5 nm grid spacing ($0.64\mu\text{m}\times0.64\mu\text{m}\times0.64\mu\text{m}$). The numerical algorithm is developed with an adaptive time step that is automatically adjusted based on the evolution rate of the phase field variables. The computational time depends on the total time of the thermal history and the richness of the simulation process (nucleation, precipitate growth, no precipitates, etc.) where the latter one dictates the maximum time step ensuring stability. The total CPU time ranges from a few minutes (points on the surface) to 30 h (points inside the component) for each RVE (4 *Intel(R) Xeon(R) CPU E5-2690 v3 @ 2.6 GHz*, 12 cores each). Note that the present work does not take into account the chemical segregation that occurs during printing and thus the initial condition for all RVEs is of the nominal composition of INCONEL 718, *i.e.* $\chi_{Al} = 0.024$ and $\chi_{Nb} = 0.038$.

The results of the precipitate simulations showing the number of nuclei of γ' precipitates within the impeller are collated in Fig. 12.

The figure shows the simulation results for the cases NS2, NS3 and NS4. In the case of the standard printing conditions (case S1), no precipitate formation was observed. Interestingly, reducing the stripe width leads to the conditions that are more favourable for the formation of precipitates. However, in both the 5 mm and the 2 mm case (seen in Fig. 12 panel A)), the number and the size of the precipitates remain small (not more than 15 in any simulated point). The upper panel of Fig. 12 also shows that the distribution of the nuclei is relatively random revealing no correlation with respect to the shape of the component.

The higher propensity to precipitate nucleation and growth is observed in the case with the increased chamber temperature. This may be attributed to spending more time in the temperature regime where precipitate nucleation is more probable (see Fig. 15 for complete thermal histories). For example, from Fig. 10, we can see that probability of precipitate nucleation is high for temperatures greater than $T = 650$ °C. For the case with standard printing conditions, we analysed the thermal histories in Appendix A at the bottom of the build as well as at the top and inside the blade. We find that the time spent above 650° varies from 24s at the bottom, 1s in the blade and 1s at the top (see Fig. 15). In contrast, for the case with chamber temperature 600 °C, the corresponding times are 64 min at the bottom, 12 min in the blade and 16 min at the top. The time spent in the high nucleation temperature range explains the differences in the precipitation behaviour observed in Fig. 12.

The panel B) in Fig. 12 displays the case in which the chamber temperature is increased to 400 °C. It is clear that for the locations at the blade and near the top of the build, no significant precipitation takes place. Thermal cycles at this location are fast and short-

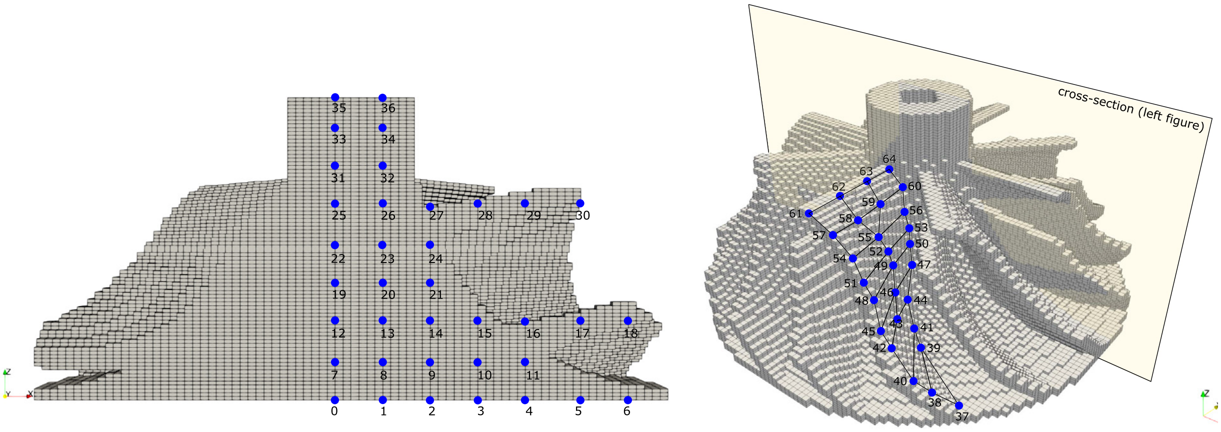

Fig. 11. Interpolation points selected for phase field simulation. Each point is described with one phase field periodic RVE modelling the evolution of γ' and γ'' precipitates. The equidistantly spaced points are selected in the cross section (left) and on one of the larger blades (right).

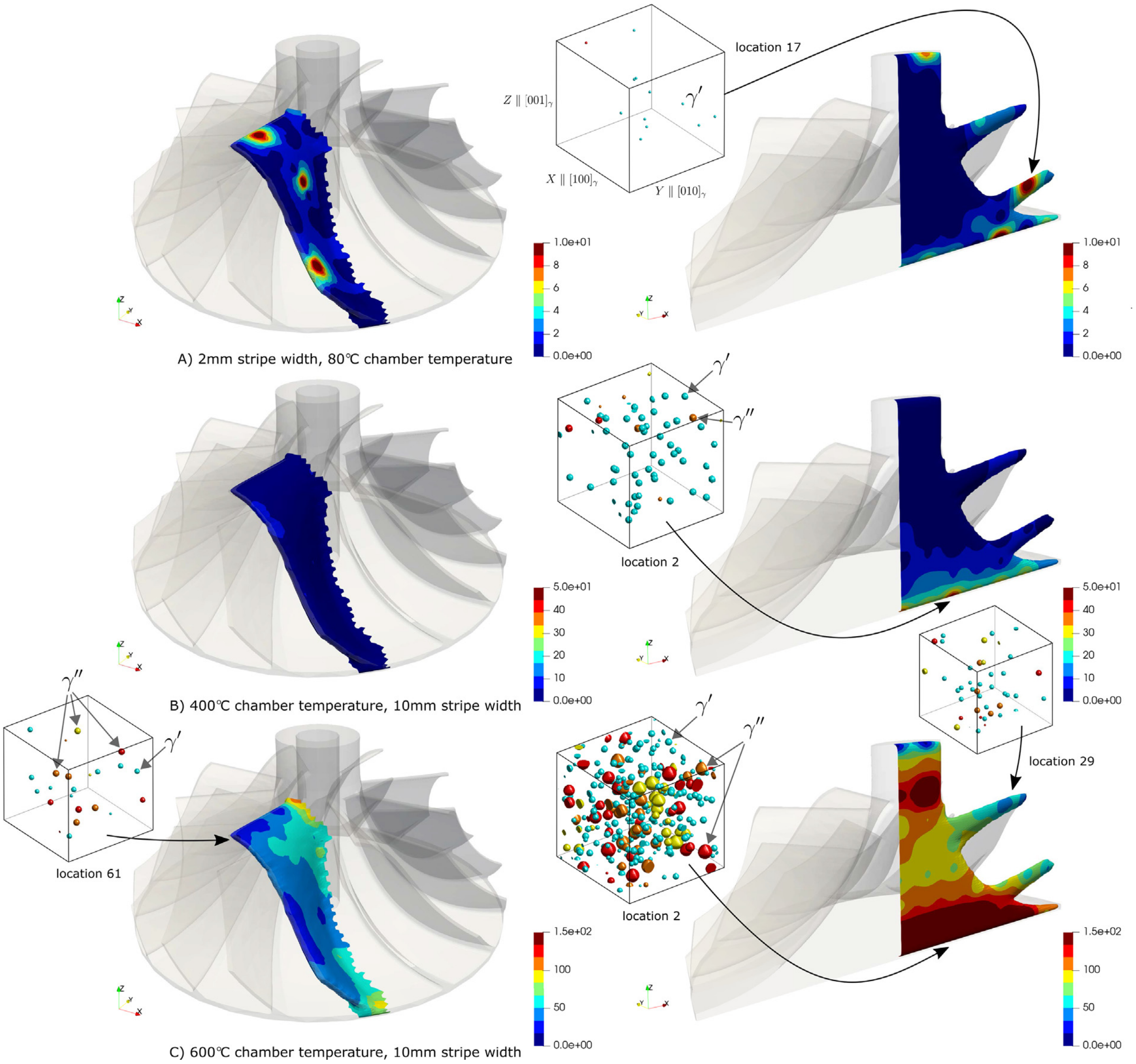

Fig. 12. Number of γ' nuclei in the as-built component for three different processing conditions: A) 2 mm stripe width, B) 400 °C chamber temperature, and C) 600 °C chamber temperature. Notice that the scale of the colorbar is different for each case to better visualize the precipitate distribution. RVEs of the phase field simulations are also shown in selected locations pointed by the arrows and location id (see Fig. 11). The possible precipitates include one γ' variant and three variants of γ''. A movie showing the precipitate evolution during the build process at location 2 for the case with chamber temperature of 600 °C is provided in supplementary information.

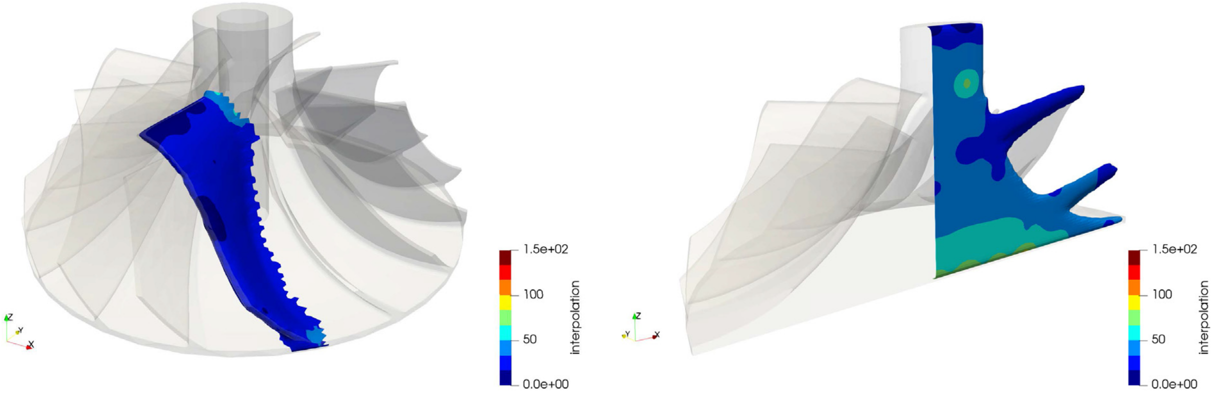

Fig. 13. Number of γ'' nuclei in the as-built component for the case with chamber temperature set to 600 °C. The γ'' nuclei are visualized in Fig. 12 case C).

lived, leading to less time being spent in temperature regimes favourable for precipitate nucleation. However, significant precipitation occurs for the locations at the bottom of the build. In this case the precipitates are still spherical and are yet to adopt the equilibrium shapes (cuboid for γ' and plate/disk for γ'').

Panel C) of Fig. 12 displays the case when the chamber temperature during the build is set to 600 °C. In this case, nucleation and growth of the precipitates dominate within the whole component. Most of the precipitates tend to form in the regions where the heat flow is dominated by conduction (bulk of the component) and only a few precipitates form in the regions where the heat flow is dominated by convection, such as the blades. It may seem slightly counter-intuitive that the gradation of the precipitates along the build direction is not linear. This can be explained by the complex shape of the impeller. In contrast to other studies [24,21], here the geometry changes with each finite element layer and transits from thin blades to a cylindrical shaft. It is also observed that, while in the lower-temperature case, most of the evolved precipitates comprise of the γ' phase, in the higher-temperature case, both γ' and γ'' precipitates form and some of the γ'' precipitates start to already adopt a non-spherical shape. The number of γ'' nuclei is in all cases found to be smaller than the number of γ' nuclei. A similar map to Fig. 12 is shown for γ'' precipitates for case C) in Fig. 13. A movie showing a detailed evolution of the precipitates for case C) location 2 is provided in the supplementary information. The movie highlights the nucleation and dissolution of precipitates as affected by the peaks in the thermal history.

In summary, on the one hand, the simulation results suggest that, for the process parameters corresponding to the default printing conditions used by commercial SLM (selective laser melting) printers, no significant precipitation occurs anywhere in the part. On the other hand, our simulations show that precipitation may be induced by changing the process parameters. However, a gradient in precipitate densities is expected due to the differences in the thermal histories experienced between the bottom and the top of the complex geometry part. Our simulation results show a qualitative agreement with a recent experimental study by Yang et al. [15] exploring the short-term heat treatment process in which the precipitates were observed during SLM. The size and shape of the precipitates, as well as the dominance of γ' over γ'' is in good agreement as well. It should also be pointed out that precipitate evolution during the printing is dominated mostly by nucleation and very little growth due to the fast heating and cooling cycles. We should remark that the gradients in precipitate fractions, as

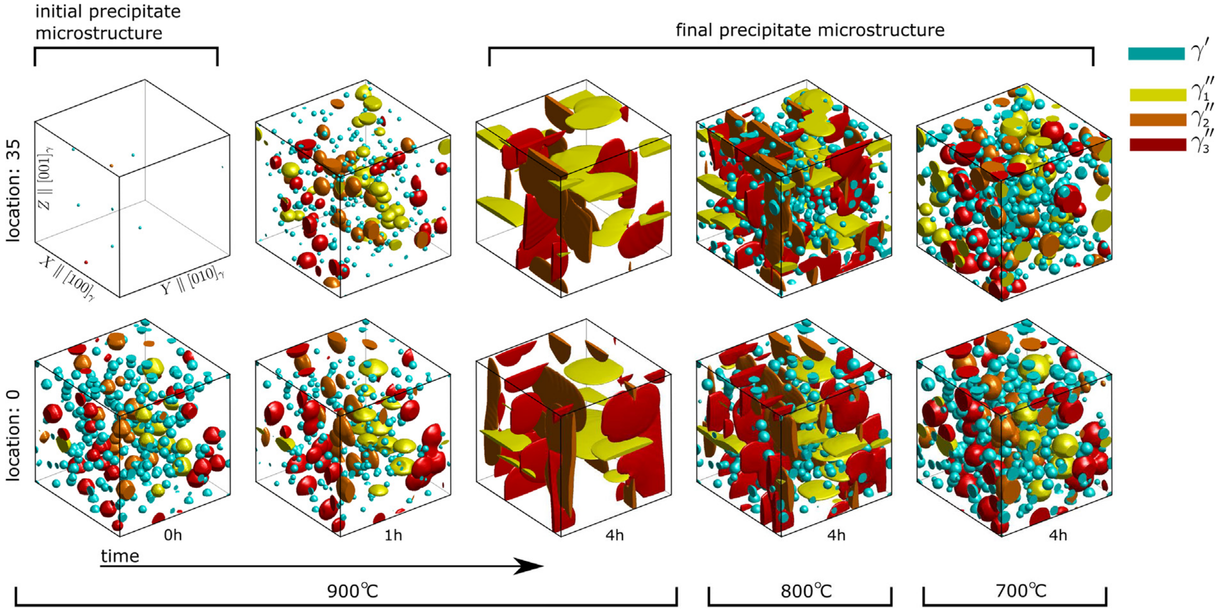

Fig. 14. Evolution of the precipitates in two locations of the impeller during the heat treatment stage. Three heat treatment simulations have been investigated: a) 900 °C, b) 800 °C, c) 700 °C. The left side of the figure displays the precipitate evolution during the heat treatment for the 900 °C case from its initial to its final configuration. The right side of the figure shows the final stage of the 800 °C and 700 °C cases.

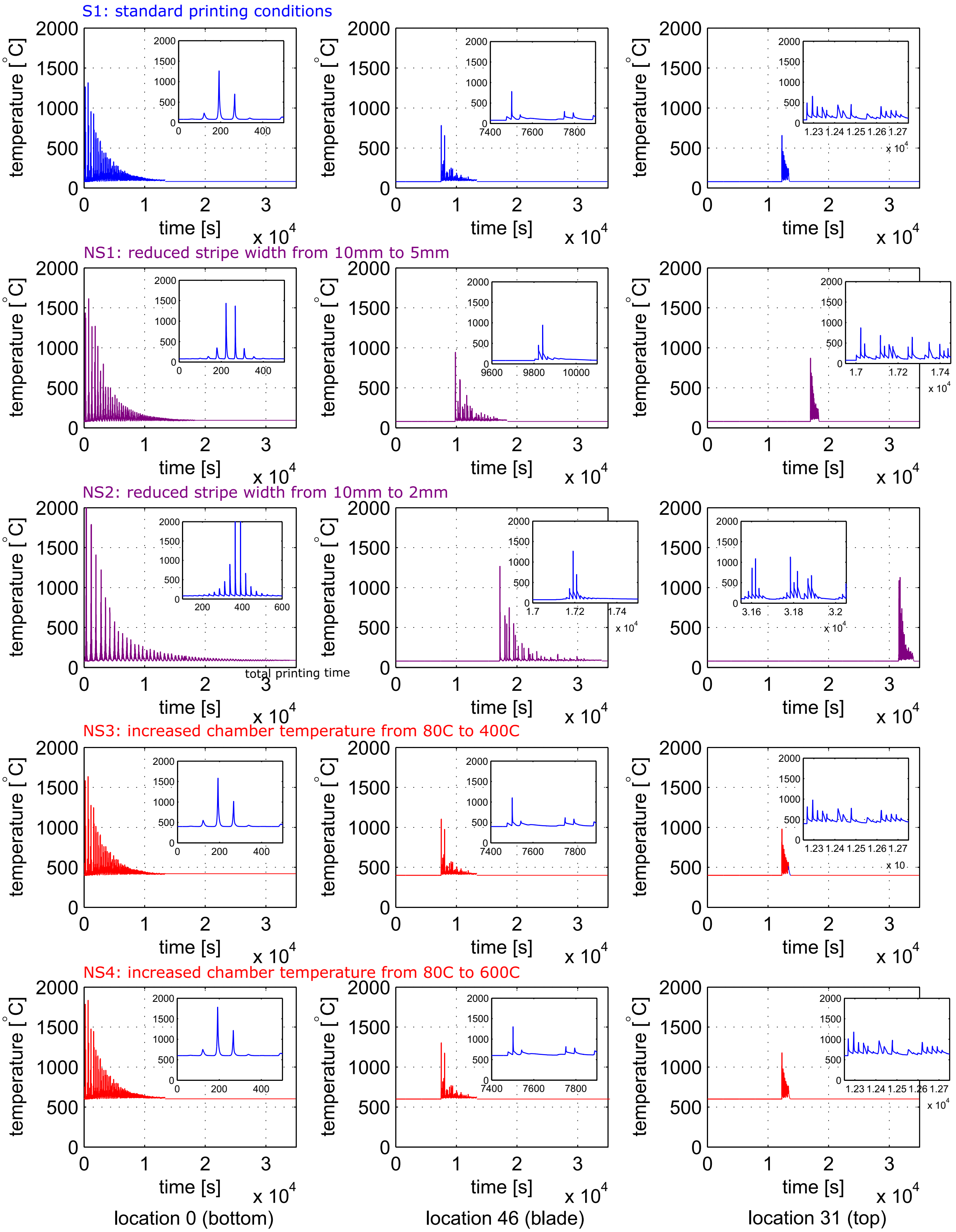
S1: standard printing conditions

NS1: reduced stripe width from 10mm to 5mm

NS2: reduced stripe width from 10mm to 2mm

NS3: increased chamber temperature from 80C to 400C

NS4: increased chamber temperature from 80C to 600C

Fig. 15. Comparison of the thermal histories for the five studied printing conditions at three distinct locations. Each row is attributed to one printing condition and each column is attributed to one interpolation node: 0, 46, and 31.

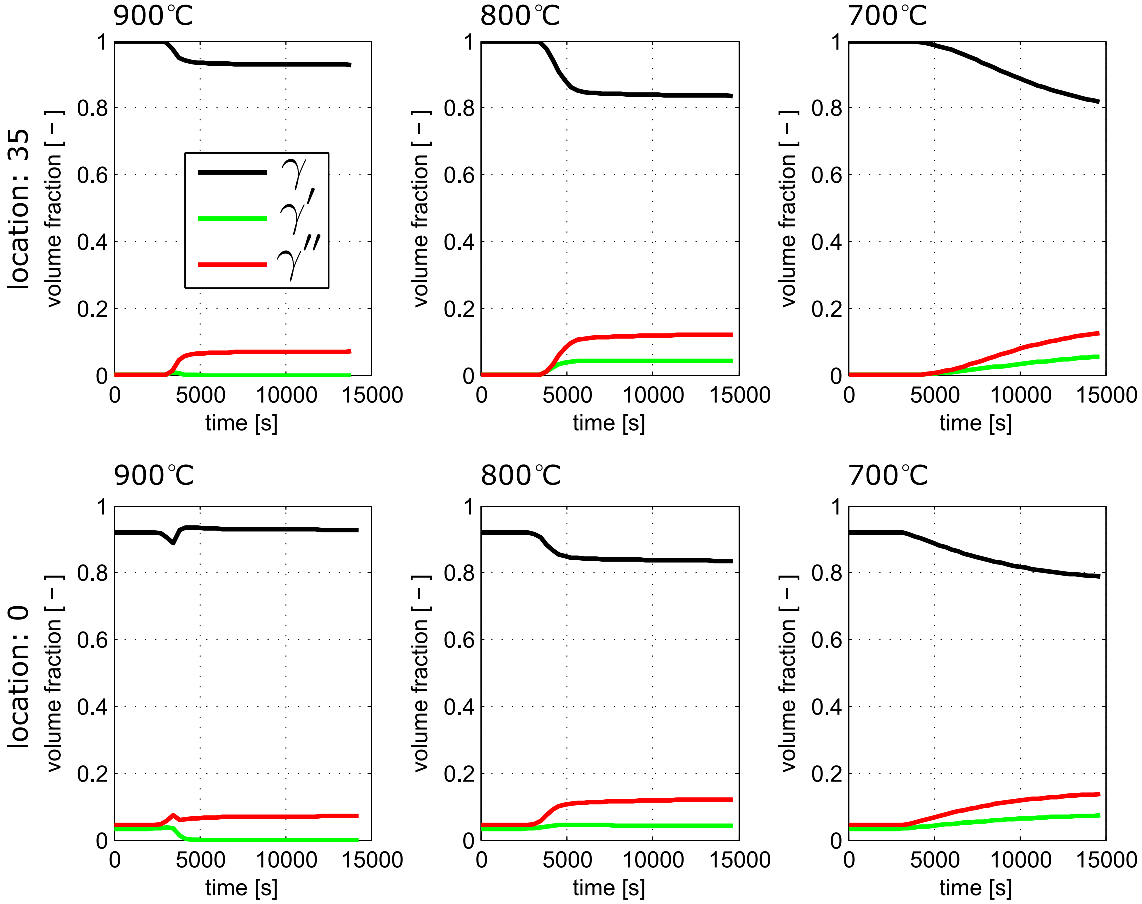

Fig. 16. Volume fraction evolution of the parent γ phase and the precipitate γ' and γ'' phases during the heat treatment simulation (see Fig. 14) at location 0 and 35. Three heat treatment cases were studied, where the temperature of the RVE is first steadily increased to (1) 900 °C, (2) 800 °C, or (3) 700 °C in the interval of 1 h and then kept constant f.or another 3 h.

well as precipitate sizes in the component, can lead to gradation in mechanical properties as well as influence the internal residual stresses.

4. Simulation of precipitate evolution during heat treatment

In order to improve the mechanical properties, as-printed parts are often subjected to a post-build heat treatment. For example, during hot isostatic pressing (HIP), as-built parts are slowly heated to high temperatures under external pressure. Motivated by such methods, we seek to understand the influence of such heat treatments on the precipitate's microstructure obtained in the previous section.

We consider the precipitate configurations from the previous printing process as the initial condition for the heat treatment simulations. We select two RVEs from the process C) in Fig. 12, one located near the bottom showing a large number of precipitate nuclei and one from the top with only a few precipitate nuclei in the as-built state. To simulate a typical heat treatment [35], the temperature for both RVEs is steadily increased from room temperature to 900 °C over a time of 1 h (heating rate ~0.25 °C/s), after which the temperature is kept constant for another 3 h. Fig. 14 on the left shows the evolution of the precipitates during the heating treatment process. The initial stage is dominated by the nucleation of the precipitates that is more pronounced in the case without precipitates. Afterwards, the precipitates evolve from being spherical to disk shaped, although γ' precipitates still appear to be spherical (1 h). Further ageing leads to a complete disappearance of γ' and transformation of γ'' into a disk-shape morphology. The disappearance of the γ' phase is consistent with the equilibrium phase diagram of IN718 [36], where γ' is stable only below 825 °C. Interestingly, the final precipitate microstructure is in both cases almost identical regardless of the initial condition.

Similar results were obtained for the heat treatment process where the temperature was steadily increased to 800 °C and 700 °C over a time of one hour and held at that temperature for another three hours. These results are shown on the right side in Fig. 14. Because of the lower heat treatment temperature ($T < 825$ °C), γ' precipitates are observed at these temperatures. However, the precipitates are still small and are yet to adopt the equilibrium shapes that decrease the misfit strain energy.

It should be remarked that although the precipitates are still growing after 4 h, the phase fractions of the phases are close to their equilibrium phase fractions defined by thermodynamics, implying that the chemical equilibrium is already established. This can be concluded by comparing the long time values of phase fractions in Fig. 16, which are consistent with the equilibrium phase diagram [36].

Based on the presented results, we may conclude, that the initial precipitate heterogeneity in the as-built component develops into a homogeneous precipitate microstructure during the heat treatment process. The evolution of the volume fraction of the parent γ phase and the γ' and γ'' precipitate phases for the three simulation cases is presented in Fig. 16 in Appendix B.

5. Conclusions

A sequential two-scale approach has been developed to study the evolution of the γ' and γ'' precipitates in IN718 at various locations of a centrifugal impeller. The presented approach enables to investigate the microstructural heterogeneity associated with the precipitates with respect to a given printing environment. Furthermore, complex geometries may be considered. The sequential multi-scale analysis consists of: (1) the finite element thermal solver at the component scale resolving the heat source at the level of a single stripe, and (2) the phase field model of γ' and γ'' precipitates. The conclusions of the investigated simulation set-ups are summarized below:

- Under standard printing conditions, no precipitation has been observed during the printing stage. This is consistent with typical SLM experiments where a post-build heat treatment is usually required to precipitate γ' and γ''.
- Reducing the stripe width is found to increase the propensity for the formation of the precipitates; however, the precipitates remain distributed randomly within the component and their size is small.
- Increased chamber temperature leads to the most suitable conditions for precipitation during the printing stage. At 400 °C, spherical precipitates of γ' phase appear in the locations inside the component. At higher temperatures of 600 °C, both γ' and γ'' precipitates form and their volume fraction starts to correlate with the geometrical features of the impeller. They mostly appear in the locations inside the component where the heat flow is trapped and dominated by conduction keeping the temperatures relatively high for longer times, and are absent in the regions such as thin blades where the heat is more quickly transferred by convection.
- The printing may result in a part level gradation of precipitate size and volume fraction. This gradation is influenced by the geometry of the part being built.
- Subsequent heat treatment simulations indicated strong homogenization of the precipitate microstructure with the final morphology, shape, size and distribution relatively uniform and independent of the initial as-built state.

Given the importance of the precipitates on the overall mechanical response [6], further extensions of the study aimed at investigation of the optimal printing strategies (such as those targeted to grain microstructures [11,37]) will likely open up novel design concepts with regard to process-induced precipitation and pave new ways for the development of gradual microstructural changes to tailor the mechanical properties in components of complex geometries.

Data availability

The data generated in the present work can be obtained from the authors on request.

Declaration of Competing Interest

The authors declare that they have no known competing financial interests or personal relationships that could have appeared to influence the work reported in this paper.

Acknowledgements

The authors would like to acknowledge the National Supercomputing Centre (NSCC) Singapore for the usage of their supercomputing facilities and the funding support by the project “Industrial Digital Design and Additive Manufacturing Workflows” (SC23/19-2087EM-IAFR).

Appendix A. Thermal histories

The following figure collates the thermal histories for the five studied printing processes in three distinct nodes of the finite element mesh. The node numbered 2960 (interpolation point 0) lies near the bottom centre of the component, 93410 (interpolation point 46) lies in the blade, and 139076 (interpolation point 31) lies near the top in the region of the shaft (see Fig. 11). The magnified figures demonstrate the thermal history variations near the first few peaks of the thermal history in the interval of 500s. The total printing time increases with reducing the stripe width. It can be seen from the figures that the highest density of the peaks is present in the bottom part of the component while the lowest density is present in the region of the blade.

Appendix B. Volume fraction evolution

The following figure illustrates the volume fraction evolution for the parent γ phase and the precipitate phases γ' and γ'' during the heat treatment simulations presented in Fig. 14. The two locations differ in the initial volume fraction of precipitates in the as-built state. In the higher temperature heat treatment case (900°), the γ' precipitates completely dissolve, while the lower temperature heat treatment cases result in a mixture of both γ' and γ'' precipitates.

Appendix C. Supplementary material

Supplementary data associated with this article can be found, in the online version, at https://doi.org/10.1016/j.matdes.2021.109851.

References

[1] D.D. Gu, W. Meiners, K. Wissenbach, R. Poprawe, Laser additive manufacturing of metallic components: materials, processes and mechanisms, Int. Mater. Rev. 57 (3) (2012) 133–164.
[2] R. Liu, Z. Wang, T. Sparks, F. Liou, J. Newkirk, 13 - aerospace applications of laser additive manufacturing, in: Milan Brandt (Ed.), Laser Additive Manufacturing, Woodhead Publishing Series in Electronic and Optical Materials, Woodhead Publishing, 2017, pp. 351–371.
[3] W.S.W. Harun, M.S.I.N. Kamariah, N. Muhamad, S.A.C. Ghani, F. Ahmad, Z. Mohamed, A review of powder additive manufacturing processes for metallic biomaterials, Powder Technol. 327 (2018) 128–151.
[4] David L. Bourell, Perspectives on additive manufacturing, Annu. Rev. Mater. Res. 46 (1) (2016) 1–18.
[5] Nikolai Arjakine, Jerry Bruck, Birgit Gruger, Dirk M Seeger, and Rolf Wilkenhoener. Advanced Weld Repair of Gas Turbine Hot Section Components, jun 2008.
[6] Saeede Ghorbanpour, Milovan Zecevic, Anil Kumar, Mohammad Jahedi, Jonathan Bicknell, Luke Jorgensen, Irene J. Beyerlein, Marko Knezevic, A crystal plasticity model incorporating the effects of precipitates in superalloys: Application to tensile, compressive, and cyclic deformation of inconel 718, Int. J. Plast 99 (2017) 162–185.
[7] E.A. Loria, Metals Minerals, Materials Society. Structural Materials Division, ASM International, National Association of Corrosion Engineers, and Nickel Development Institute (Canada). Superalloys 718, 625, 706 and Various Derivatives: Proceedings of the International Symposium on Superalloys 718, 625, 706 and Various Derivatives: Held June 17–20, 2001. TMS, 2001.
[8] Tresa M. Pollock, Sammy Tin, Nickel-based superalloys for advanced turbine engines: Chemistry, microstructure and properties, J. Propul. Power 22 (2) (2006) 361–374.
[9] A.F. Rowcliffe, L.K. Mansur, D.T. Hoelzer, and R.K. Nanstad. Perspectives on radiation effects in nickel-base alloys for applications in advanced reactors. Journal of Nuclear Materials, 392(2), 341–352, 2009. Nuclear Fuels and Structural Materials 2.
[10] G. Appa Rao, Mahendra Kumar, M. Srinivas, D.S. Sarma, Effect of standard heat treatment on the microstructure and mechanical properties of hot isostatically pressed superalloy inconel 718, Materials Science and Engineering: A 355 (1) (2003) 114–125.

[11] H. Helmer, A. Bauereiß, R.F. Singer, C. Körner, Grain structure evolution in inconel 718 during selective electron beam melting, Materials Science and Engineering: A 668 (2016) 180–187.

[12] Yunhao Zhao, Kun Li, Matthew Gargani, Wei Xiong, A comparative analysis of inconel 718 made by additive manufacturing and suction casting: Microstructure evolution in homogenization, Additive Manufacturing 36 (2020) 101404.

[13] Tahira Raza, Joel Andersson, and Lars-Erik Svensson. Microstructure of selective laser melted alloy 718 in as-manufactured and post heat treated condition. Procedia Manufacturing, 25:450–458, 2018. Proceedings of the 8th Swedish Production Symposium (SPS 2018).

[14] Hong-Yuan Wan, Zhong-Jiao Zhou, Chang-Peng Li, Guo-Feng Chen, Guang-Ping Zhang, Enhancing fatigue strength of selective laser melting-fabricated inconel 718 by tailoring heat treatment route, Adv. Eng. Mater. 20 (10) (2018) 1800307.

[15] Huihui Yang, Jingjing Yang, Wenpu Huang, Guanyi Jing, Zemin Wang, Xiaoyan Zeng, Controllable in-situ aging during selective laser melting: Stepwise precipitation of multiple strengthening phases in inconel 718 alloy, Journal of Materials Science & Technology 35 (9) (2019) 1925–1930.

[16] William E. Frazier, Metal additive manufacturing: A review, Metal Additive Manufacturing: A Review 23 (6) (Apr 2014) 1917–1928.

[17] W.E. King, A.T. Anderson, R.M. Ferencz, N.E. Hodge, C. Kamath, S.A. Khairallah, A.M. Rubenchik, Laser powder bed fusion additive manufacturing of metals; physics, computational, and materials challenges, Applied Physics Reviews 2 (4) (2015) 041304.

[18] N.E. Hodge, R.M. Ferencz, J.M. Solberg, Implementation of a thermomechanical model for the simulation of selective laser melting, Comput. Mech. 54 (1) (July 2014) 33–51.

[19] N.E. Hodge, R.M. Ferencz, and R.M. Vignes. Experimental comparison of residual stresses for a thermomechanical model for the simulation of selective laser melting. Additive Manufacturing, 12:159–168, 2016. Special Issue on Modeling & Simulation for Additive Manufacturing.

[20] Michael F. Zaeh, Gregor Branner, Investigations on residual stresses and deformations in selective laser melting, Prod. Eng. Res. Devel. 4 (2010) 35–45.

[21] Magnus J. Anderson, Chinnapat Panwisawas, Yogesh Sovani, Richard P. Turner, Jeffery W. Brooks, Hector C. Basoalto, Mean-field modelling of the intermetallic precipitate phases during heat treatment and additive manufacture of inconel 718, Acta Mater. 156 (2018) 432–445.

[22] Patcharapit Promoppatum, P. Shi-Chune Yao, Chris Pistorius, Anthony D. Rollett, Peter J. Coutts, Frederick Lia, Richard Martukanitz, Numerical modeling and experimental validation of thermal history and microstructure for additive manufacturing of an inconel 718 product, Progress in Additive Manufacturing 3 (2016) 15–32.

[23] Xu Song, Stefanie Feih, Wei Zhai, Chen-Nan Sun, Feng Li, Raj Maiti, Jun Wei, Yangzhan Yang, Victor Oancea, Leon Romano Brandt, and Alexander M. Korsunsky. Advances in additive manufacturing process simulation: Residual stresses and distortion predictions in complex metallic components. Materials & Design, 193:108779, 2020.

[24] H.C. Basoalto, C. Panwisawas, Y. Sovani, M.J. Anderson, R.P. Turner, B. Saunders, and J.W. Brooks. A computational study on the three-dimensional printability of precipitate-strengthened nickel-based superalloys. Proceedings of the Royal Society A: Mathematical, Physical and Engineering Sciences, 474 (2220):20180295, 2018.

[25] N. Zhou, D.C. Lv, H.L. Zhang, D. McAllister, F. Zhang, M.J. Mills, Y. Wang, Computer simulation of phase transformation and plastic deformation in in718 superalloy: Microstructural evolution during precipitation, Acta Mater. 65 (2014) 270–286.

[26] Caleb O. Yenusah, Yanzhou Ji, Yucheng Liu, Tonya W. Stone, Mark F. Horstemeyer, Long-Qing Chen, Lei Chen, Three-dimensional phase-field simulation of γ'' precipitation kinetics in inconel 625 during heat treatment, Comput. Mater. Sci. 187 (2021) 110123.

[27] Robert Laskowski, Kun Wang, Rajeev Ahluwalia, Kewu Bai, Guglielmo Vastola, Yong-Wei Zhang, Phase field model for multiphase alloys under arbitrary thermal history: An application to in718 super-alloy, J. Alloy. Compd. 861 (2021) 158630.

[28] Centrifugal impeller. https://grabcad.com/library/centrifugal-impeller–1.

[29] W. Schroeder, K. Martin, B. Lorensen, Inc Kitware, The Visualization Toolkit: An Object-oriented Approach to 3D Graphics, Kitware (2006).

[30] The Trilinos Project Team. The Trilinos Project Website.

[31] T.W. Eagar, N.S. Tsai, Temperature fields produced by traveling distributed heat sources, Weld. Res. Suppl.; (United States) 12 (1983).

[32] Seong Gyoon Kim, Won Tae Kim, and Toshio Suzuki. Phase-field model for binary alloys. Phys. Rev. E, 60:7186–7197, Dec 1999.

[33] Jan-Olof Andersson, John Ågren, Models for numerical treatment of multicomponent diffusion in simple phases, J. Appl. Phys. 72 (4) (1992) 1350–1355.

[34] Elastic constants. https://materialsproject.org/.

[35] Benedikt Diepold, Nora Vorlaufer, Steffen Neumeier, Thomas Gartner, Mathias Göken, Optimization of the heat treatment of additively manufactured Ni-base superalloy IN718, International Journal of Minerals, Metallurgy, and Materials 27 (5) (May 2020) 640–648.

[36] Fan Zhang, Weisheng Cao, Chuan Zhang, Shuanglin Chen, Jun Zhu, and Duchao Lv. Simulation of co-precipitation kinetics of γ' and γ'' in superalloy 718. In Eric Ott, Xingbo Liu, Joel Andersson, Zhongnan Bi, Kevin Bockenstedt, Ian Dempster, Jon Groh, Karl Heck, Paul Jablonski, Max Kaplan, Daisuke Nagahama, and Chantal Sudbrack, editors, Proceedings of the 9th International Symposium on Superalloy 718 & Derivatives: Energy, Aerospace, and Industrial Applications, pages 147–161, Cham, 2018. Springer International Publishing.

[37] Naresh Nadammal, Sandra Cabeza, Tatiana Mishurova, Tobias Thiede, Arne Kromm, Christoph Seyfert, Lena Farahbod, Christoph Haberland, Judith Ann Schneider, Pedro Dolabella Portella, and Giovanni Bruno. Effect of hatch length on the development of microstructure, texture and residual stresses in selective laser melted superalloy inconel 718. Materials & Design, 134:139–150, 2017.